Designer Exosomes for Active Targeted Chemo-Photothermal Synergistic Tumor Therapy

Jie Wang, Yue Dong, Yiwei Li, Wei Li, Kai Cheng, Yuan Qian, Guoqiang Xu, Xiaoshuai Zhang, Liang Hu, Peng Chen, Wei Du, Xiaojun Feng, Yuan-Di Zhao, Zhihong Zhang, and Bi-Feng Liu*

Exosomes, naturally derived nanovesicles secreted from various cell types, can serve as an effective platform for the delivery of various cargoes, because of their intrinsic ability such as long blood circulation and immune escaping. However, unlike conventional synthetic nanoparticles, drug release from exosomes at defined targets is not controllable. Moreover, endowing exosomes with satisfactory cancer-targeting ability is highly challenging. Here, for the first time, a biological and synthetic hybrid designer exosome is described with photoresponsive functionalities based on a donor cell-assisted membrane modification strategy. Practically, the designer exosome effectively accumulates at target tumor sites via dual ligand-mediated endocytosis. Then the localized hyperthermia induced by the conjunct gold nanorods under near-infrared irradiation impacts the permeability of exosome membrane to enhance drug release from exosomes, thus inhibiting tumor relapse in a programmable manner. The designer exosome combines the merits of both synthetic materials and the natural nanovesicles. It not only preserves the intrinsic functionalities of native exosome, but also gains multiple abilities for efficient tumor targeting, controlled release, and thermal therapy like synthetic nanocarriers. The versatile designer exosome can provide functional platforms by engineering with more multifarious functionalities from synthetic materials to achieve individualized precise cancer therapy in the future.

1. Introduction

Cancer is the world's most devastating disease, and for the purpose to cure it, one of the cancer treatment methods being used most widely is chemotherapy. A branch of artificial nanoparticles modified with several targeting moieties for hyperthermal therapy provides the possibility of selective delivering chemotherapeutic drugs to tumor cells with high drug penetration efficiency and therapeutic efficacy.[1] However, significant obstacles still remain. These nonself materials are not stable enough in bloodstream.[2] They may also cause adverse effects, such as activating oxidative stress pathways.[3] In recent years, synthetic thermosensitive liposomes conjugated gold nanorods for targeted chemo-photothermal synergistic tumor therapy with fewer side effects have been developed.[4] However, the preparation of synthetic thermosensitive liposomes is complex and time-consuming. The cost is also high. Exosomes are nanosized membrane vesicles (50–150 nm in diameter) released by cells and easily available by isolating these from bodily fluids and cell culture supernatants.[5] The considerable attention that these vesicles have recently attracted is due to their intercellular communication role, which involves transporting molecules, for instance, proteins, lipids, as well as RNAs among cells.[6,7] Exosomes are an outstanding drug platform for delivery for the reason that they have excellent biocompatibility, near nonimmunogenicity, and long blood circulation ability, all of which result from their endogenous origin.[8,9] Moreover, exosomes also can traverse the blood–brain barrier,[10,11] penetrate dense structural tissue.[12] Exosomes have special surface composition and their origin is endogenous, so their life circulation is greater than those of liposomes.[13] However, endowing exosomes with satisfactory cancer-targeting ability is highly challenging and thus has rarely been reported. Moreover, developing a method for the controlled release of drugs encapsulated in exosomes is a problem that has not yet been addressed.

One interesting biological strategy to equip exosomes with targeting properties involves incorporating targeting peptides or proteins into exosomes by inducing their expression in

J. Wang, Y. Dong, W. Li, K. Cheng, Dr. Y. Qian, G. Xu, X. Zhang,
Dr. P. Chen, Prof. W. Du, Prof. X. Feng, Prof. Y.-D. Zhao,
Prof. Z. Zhang, Prof. B.-F. Liu
The Key Laboratory for Biomedical Photonics of MOE
at Wuhan National Laboratory for Optoelectronics—Hubei
Bioinformatics & Molecular Imaging Key Laboratory
Department of Biomedical Engineering
College of Life Science and Technology
Huazhong University of Science and Technology
Wuhan 430074, China
E-mail: bfliu@mail.hust.edu.cn
Dr. Y. Li
Department of Mechanical Engineering
Massachusetts Institute of Technology
Cambridge, MA 02139, USA
Dr. L. Hu
Brain Research Center
Wuhan Institute of Physics and Mathematics
Chinese Academy of Sciences
Wuhan 430071, China

The ORCID identification number(s) for the author(s) of this article
can be found under https://doi.org/10.1002/adfm.201707360.

exosome donor cells through strict and complicated genetic manipulation.[8,10,14] In addition to ligand-mediated targeting, magnetic drug targeting provides an alternative method, which is noninvasive, to improve the level of therapeutic efficacy.[15] However, to accurately target the deep tissues of the human body is difficult, besides, the target efficacy is dependent not only on the properties of the magnetic iron oxide nanoparticles but also on the shell choice, drug linkage type, and blood flow rate.[16] For all the methods mentioned above, the targeting efficiency of a single ligand is not often very good because of a phenomenon named as receptor saturation.[17] To overcome these limitations, dual ligand based active targeting strategies can be utilized to further improve the efficiency of targeting through the individual ligands' cooperative effect. Moreover, stimuli responsiveness can be explored to enable exosomes to spatiotemporally release therapeutic agents at a target tumor site on demand. The active targeting and stimuli-responsive characteristics of the engineered exosomes can not only facilitate their specific accumulation at tumor sites but also improve the drug release at the target tumor site, which can enhance therapeutic efficacy and alleviate side effects.[18] Therefore, developing a new exosome-based delivery platform capable of simultaneous targeted delivery and controlled drug release is highly desirable. To date, various gold nanomaterials, including gold nanoshells, gold nanorods (AuNRs), and gold nanocages, have been shown to absorb light in the NIR region (700–900 nm) and kill cancer cells locally without harming the healthy tissues via transforming optical energy into heat.[19] These nanomaterials show promise for biomedical applications, especially tumor therapy. Among them, AuNRs exhibit a narrow size distribution and can penetrate tumors more rapidly than nanospheres because they can readily torque and tumble. In this work, we designed the first strategy based on combining AuNRs with exosomes for tumor-targeted chemo-photothermal therapy. Previous studies have reported that the amphiphilic molecule 1,2-dioleoyl-sn-glycero-3-phosphoethanolamine-poly(ethylene glycol) (DSPE-PEG) could assemble itself into the phospholipid layer of cells.[20] In this strategy (**Scheme 1**), we generated exosomes by culturing donor cells in medium containing arginyl–glycyl–aspartic acid (RGD)-functionalized DSPE-PEG (DSPE-PEG-RGD) and sulfhydryl-functionalized DSPE-PEG (DSPE-PEG-SH) as our previous studies.[21] Thus, the membrane of the donor cells was modified with RGD and sulfhydryl groups. Exosomes could also be modified with RGD and sulfhydryl groups (RGD-Exos-SH). Then, AuNRs could be easily combined with exosomes through the formation of Au—S bonds. Furthermore, to improve the tumor cellular uptake efficiency, the surface of AuNR@RGD-Exos was functionalized with another tumor-specific targeting ligand (folic acid, FA) through covalent bonds. Despite the fact that the FA and RGD's synergistic effect on the targeted tumor nanoparticles have previously been reported,[22] their applications to the tumor targeting of exosomes have not been systematically studied. We further compared the synergistic effect of the dual ligand
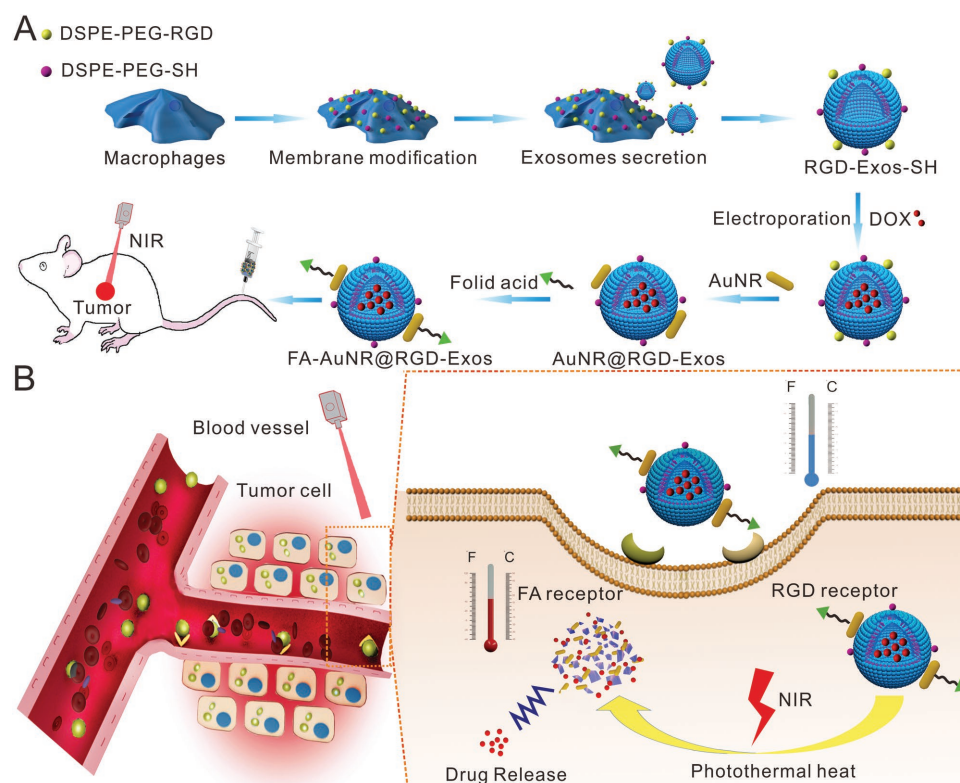
Scheme 1. A) Schematic illustration of the design of FA-AuNR@RGD-DOX-Exos and their antitumor effect under NIR irradiation. The therapeutic efficiency of FA-AuNR@RGD-DOX-Exos was evaluated in a tumor-bearing mouse model. B) Schematic illustration of FA-AuNR@RGD-DOX-Exos as a robust nanoplatform for targeted delivery and chemo-photothermal synergistic tumor therapy.

**ADVANCED
SCIENCE NEWS**
www.advancedsciencenews.com

**ADVANCED
FUNCTIONAL
MATERIALS**
www.afm-journal.de

targeting of exosomes with a single ligand strategy. Because of the synergistic effect of the dual ligands, a high local exosome concentration could accumulate at the tumor site, generating better therapeutic outcomes. It is well known that the localized hyperthermia induced by AuNRs under near-infrared irradiation can impact the permeability of cell membrane by enhancing the mobility of lipid molecules and creating rigid hydrophilic pores because integral glycoproteins on the membrane can undergo thermal denaturation under the local heat.[23] Exosomes will acquire this thermosensitivity. Previous studies have reported that high temperatures ($T = 40\ °C$) can disrupt the exosome membrane and promote fusion.[24] Thus, we speculated that laser-induced hyperthermia could result in exosome membrane instability and thus encapsulated drug release would be promoted. This drug release behavior, which is NIR-enhanced, could be rapidly, selectively, and locally activated by remote stimuli.[25] Meanwhile, NIR-induced hyperthermia dramatically improves the cancer cell uptake of the released drug by promoting the gel-to-liquid crystalline phase transition of cell membrane.[26] Furthermore, because tumor cells have a lower heat tolerance than normal cells, localized hyperthermia would selectively eliminate the tumor cells without affecting surrounding normal tissues.[27]

To demonstrate the potential of this strategy, the efficiency of targeted drug delivery and the exosomes' effect in terms of photothermal chemotherapeutic, which are administered through intravenous injection in tail vein, were being evaluated in nude mice bearing tumor cell xenografts. This strategy opens a new avenue for engineering exosomes with promising drug delivery functions for precise chemo-photothermal tumor therapy; it also aims at improving the therapeutic efficacy as well as reducing side effects.

2. Results and Discussion

2.1. Preparation and Characterization of FA-AuNR@RGD-Exos

We demonstrated a reproducible and bio-friendly strategy to combine AuNRs with engineered exosomes via a donor cell-assisted membrane modification strategy. Herein, we proposed using sulfhydrylated exosomes as a platform for efficiently conjugating natural exosomes with AuNRs by forming Au—S bonds. Through the same strategy, the exosomes can be equipped with targeting biomolecules. RGD, the specific ligand recognition site of integrins, has a certain affinity for combining with integrins overexpressed on the tumor neovasculature and tumor cells.[28] Thus, we proposed that RGD modification could endow the exosomes with more precise tumor targeting properties. Functionalized donor cells must be developed to obtain the modified exosomes. Several studies have demonstrated that cancer cells could secret exosomes into the tumor microenvironment and breast tumor-derived exosomes can stimulate metastasis and contribute to forming a niche to promote tumor growth.[29] It illustrated that exosomes were cell-to-cell transferable. They could deliver bioactive molecules within cells and could cross physiological barriers and extravasate from tumor vessels as well as following-up diffuse into tumor tissues. Therefore, exosomes can be exploited as natural drug delivery carrier. However, cancer cells-derived exosomes commonly do not possess tumor targeting capability to relevant tumors and may influence their therapy efficacy during complicated therapy procedures to some extent. In this work, we used THP-1 macrophages cell as our donor cell (normal cell) for producing exosomes. Macrophages have been reported that can be recruited by the cytokines released from tumor tissues[30] and macrophage derived exosomes have been demonstrated that could inherent this intrinsic tumor targeting property by maintaining the topology of plasma membrane proteins and avoid entrapment in mononuclear phagocytes in several studies.[31] The macrophages were incubated with DSPE-PEG-SH ($0–50\ \mu g\ mL^{-1}$) and/or DSPE-PEG-RGD ($0–5\ \mu g\ mL^{-1}$, 1/10 of DSPE-PEG-SH) for 2 d to obtain SH-functionalized and/or RGD-functionalized donor cells. As shown in Figure S1 (Supporting Information), the nuclear magnetic resonance (NMR) result showed that SH and RGD had been modified on donor cells. Then, the functionalized cells were stressed by culturing them in medium containing 10% exosome-free fetal bovine serum (FBS) to enhance the release of exosomes. Next, by using a previously reported differential centrifugation protocol, the exosomes can be separated from the conditioned medium. The Western blot result showed that there was almost no change in the GAPDH protein number of exosomes before and after modification (Figure S2, Supporting Information). It suggested that our modification process would not damage the original properties of exosomes. We incubated the engineered exosomes with AuNRs for 20 h (on a shaking incubator) and assembled them with FA which was used as the targeting moiety at room temperature. FA tends to bind to the FR (folate receptor) selectively which is overexpressed in cancer cells.[32] The characterization of the exosomes is shown in Figure S3 (Supporting Information). Two typical exosome marker proteins (CD81 and CD63) were observed using flow cytometry and the negative exosome marker protein (Calnexin) was tested by Western blot (Figure S4, Supporting Information), indicating that the vesicles were macrophage-derived exosomes. The standard exosomes amount was $4.2 × 10^7$ particles mL^{-1} and the total protein concentration of our standard exosomes was $1.337\ mg\ mL^{-1}$ (Figure S5, Supporting Information). We diluted it ten times for electron microscope and dynamic light scattering analyses. Comparing the morphologies and the hydrodynamic diameters of the purified exosomes, the engineered exosomes (RGD-Exos-SH) and the AuNR-functionalized exosomes conjugated with FA and RGD (FA-AuNR@RGD-Exos) are shown in **Figure 1**A. It revealed the feasibility of combining AuNRs and the engineered exosomes. Transmission electron microscopy (TEM) image of AuNR was shown in Figure S6 (Supporting Information). Compared with the unmodified exosomes, the hydrodynamic diameter of RGD-Exos-SH was nearly unchanged, indicating that exosome membrane modification did not influence the size of the exosomes and that this donor cell-assisted modification strategy was biocompatible. Moreover, the mean size of FA-AuNR@RGD-Exos was 150–300 nm, thus enabling these exosomes to accumulate at solid tumors, via the enhanced permeability and retention (EPR) effect, which is caused in poor lymphatic drainage of cancer sites and by the leaky vasculature. The TEM images showed that the AuNRs were attached to the engineered exosomes, corroborating the strong interaction between the
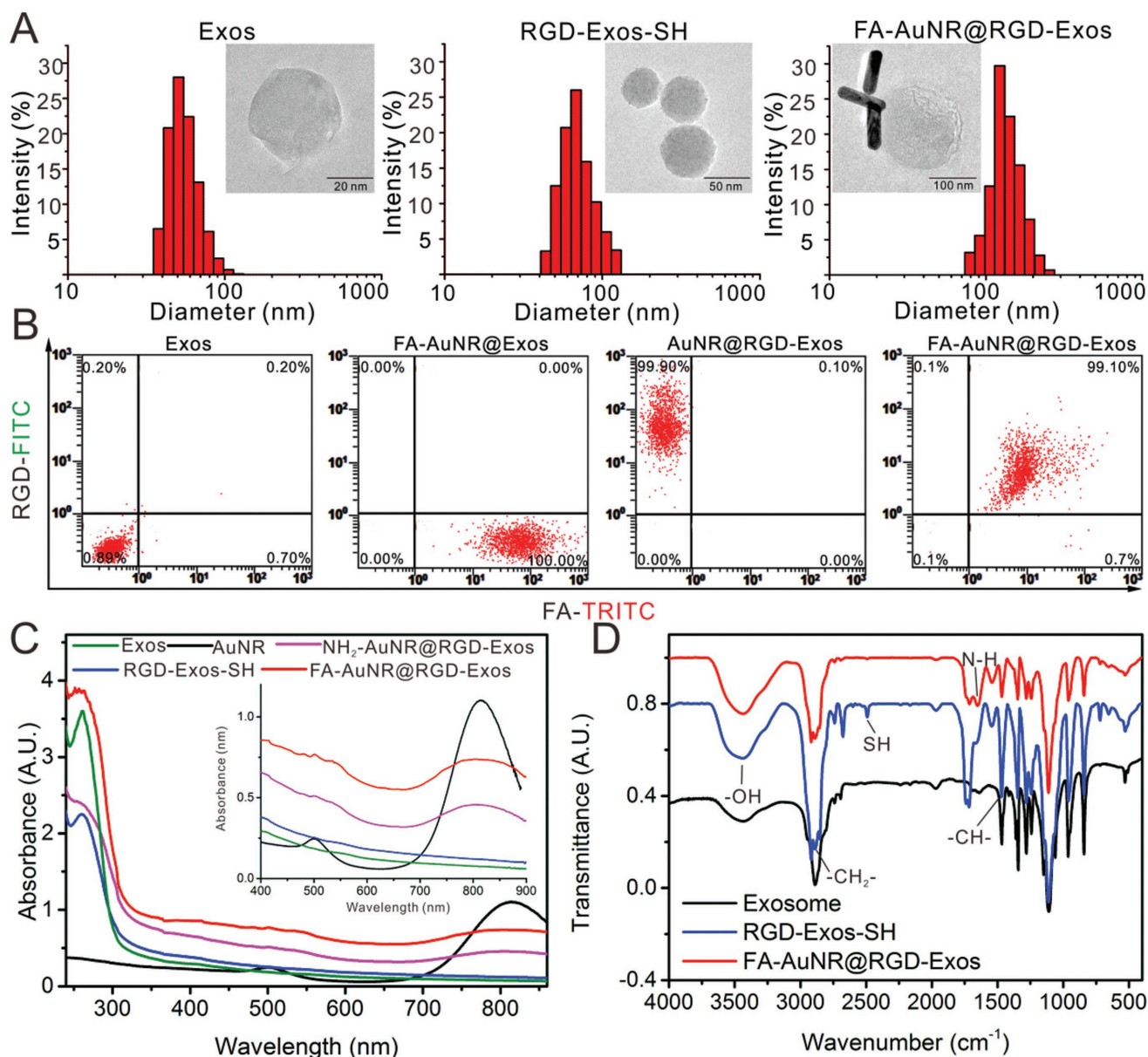
Figure 1. Characterization of FA-AuNR@RGD-DOX-Exos. A) Hydrodynamic diameter and TEM images of the unmodified exosomes, RGD-Exos-SH and FA-AuNR@RGD-Exos. B) The FA and RGD on the unmodified exosomes, FA-AuNR@Exos, AuNR@RGD-Exos, and FA-AuNR@RGD-DOX-Exos, were determined by flow cytometry. C) UV–vis spectra of the unmodified exosomes, AuNR-, RGD-, and sulfhydryl-functionalized exosomes (RGD-Exos-SH), NH₂-AuNR@RGD-Exos and FA-AuNR@RGD-Exos. The inset shows the magnified UV–vis spectra from 400 to 900 nm. D) Fourier-transform infrared spectroscopy (FTIR) analysis of the unmodified exosomes, RGD- and sulfhydryl-functionalized exosomes (RGD-Exos-SH) and FA-AuNR@RGD-Exos.

AuNR and the exosomes. As shown in Figure S7 (Supporting Information), we could confirm that there was no aggregation of our engineered exosomes. We determined the amount of AuNRs binded per exosome according to previous reported study.[33] According to column fractions and UV–vis characterization from the eluted fractions, it can be determined that at least 70% of the AuNRs were associated with exosome hybrids.

This result was consistent with TEM images of AuNR@Exos. The elemental composition of the AuNR@Exos was determined by performing energy dispersive X-ray spectroscopy measurements on the TEM data, as shown in

Figure S8 (Supporting Information). The changes in surface zeta potential of the FA-AuNR@RGD-Exos further confirmed that the exosomes were modified with FA and AuNRs (Figure S9, Supporting Information). About the complex surface, of which the zeta potential varied from negative to positive, followed AuNR functionalization, and then changed to negative after FA functionalization. Negatively charged nanocarriers have been demonstrated to have better tumor penetration.[20] We diluted FA to different concentrations to obtain its standard concentration curve by UV–vis. Then we calculated the amount of FA binded to AuNR

**ADVANCED
SCIENCE NEWS**
www.advancedsciencenews.com

**ADVANCED
FUNCTIONAL
MATERIALS**
www.afm-journal.de

by testing our engineered exosome complex's absorbance at 280 nm. There was nearly 1.2×10^{-6} M FA that could bind to AuNR in this work. The FA modification efficiency could reach to nearly 80%. To further assess the efficiency of dual ligand modification, the FA-AuNR@RGD-Exos was incubated with RGD and FA antibodies for 30 min. After removing the excess free antibodies via sucrose gradient centrifugation, the FA-AuNR@RGD-Exos were analyzed via flow cytometry. As shown in Figure 1B, RGD and FA were efficiently and concurrently attached to the nanocarriers, yielding 99.10% double positive nanocarriers (denoted as FA-AuNR@RGD-Exos).

As shown in Figure 1C, the purified exosomes and RGD-Exos-SH did not exhibit an absorption band in the NIR region, whereas AuNR, NHS-AuNR@RGD-Exos, and FA-AuNR@RGD-Exos showed a broad absorption band in the NIR region. As the transverse and longitudinal resonance wavelengths of the AuNR-exosome complex were different from those of unmodified AuNRs, the interaction between the AuNRs and the exosomes was confirmed. Moreover, the UV–vis spectrum of the FA-AuNR@RGD-Exos showed a characteristic absorption peak of FA at 280 nm, whereas the NH_2-AuNR@RGD-Exos exhibited no obvious peak, indicating that FA had been incorporated on the AuNR@RGD-Exos through a covalent bond. The spectrum of Fourier transform infrared spectroscopy illustrates the pure exosomes and FA-AuNR@RGD-Exos was obtained to investigate the interactions between the exosomes, AuNRs, sulfhydryl groups, and dual ligands. The complex absorption bands of 1346.81 cm^{-1} from the RGD-Exos-SH (shearing the vibration of −CH−), 2491.98 cm^{-1} (stretching vibration of SH), 2889.24 cm^{-1} (stretching vibration of −CH_2−), and 3438.13 cm^{-1} (stretching vibration of O−H) shown in Figure 1D supported the successful modification of the exosomes with DSPE-PEG-RGD and DSPE-PEG-SH. The disappearance of the SH stretching vibrations in the FA-AuNR@RGD-Exos spectrum verified Au−S bond formation and thus clearly proved that the AuNRs were attached to the surface of the engineered exosomes. Moreover, the absorption band which was observed at 1652.29 cm^{-1} supported the evidence of the existence of FA on the surface of the AuNR@RGD-Exos.

2.2. Synergistic Photothermal and Chemotherapy Efficiency of AuNR@DOX-Exos

Next, we investigated the photothermal activity of AuNR@Exos by monitoring the laser-induced change in regional temperature (**Figure 2**A). After 10 min of laser irradiation (808 nm, 1.0 W cm^{-2}), the solution of AuNR@Exos, whose temperature dramatically increased within 6 min and reached 47.1 °C at 10 min (Figure 2B). Exosomes that bud from a cell membrane are known to inherit the cell membrane thermosensitivity. Thus, we proposed that the AuNR-conjugated exosomes could convert NIR light energy to heat energy, which in turn could destabilize the exosome membrane and increase drug release (Figure 2C). Next, we loaded doxorubicin (DOX) into the AuNR@Exos by electroporation. The electroporation efficiency under different initial DOX concentration was shown in Figure S10 (Supporting Information). The result showed that the packaging efficiency grew slowly with the initial

concentration of DOX increased and finally reached at a plateau of 79%. The TEM images of engineered exosomes after electroporation showed that the structure of exosomes was still intact and electroporation did not affect the ability of exosomes conjugated with AuNRs (Figure S11, Supporting Information). We measured the stability of our engineered exosomes (Figure S12, Supporting Information) and we further confirmed that DSPE-PEGs still maintain to bind on exosomal membrane after 24 h by NMR analysis (Figure S13, Supporting Information). We further verified the thermosensitivity and potential permeability of the engineered exosome membrane by testing the phase transition temperatures of the engineered exosomes (Figure S14, Supporting Information). The change in membrane permeability of the exosomes could enhance the release of entrapped drug. These data were in coincidence with our assumptions that exosomes membrane can be permeable by AuNR-induced hyperthermia under irradiation.

As shown in Figure 2D, we tested the concentration of released DOX using a standard curve. The drug release rate of AuNR@DOX-Exos with different NIR irradiation conditions is shown in Figure S15 (Supporting Information). Moreover, we studied the effects of pH and NIR light irradiation on DOX release using the dynamic dialysis method (Figure 2E). It showed that under the acidic condition of pH 5.5, the rate of drug release increased significantly compared with the condition of pH 7.4. It released a small amount of drug at pH 7.4 and exhibited relatively rapid and burst release at pH 5.5. However, the released rate of AuNR@Exos was slower than exosome under different pH conditions; this was probably because the AuNRs attached on exosome membrane helped to delay the drug release from the exosomes. The drug release rates of AuNR@DOX-Exos were significantly increased under acidic conditions because lowering the pH resulted in DOX protonation and accelerated DOX release. After 12 h, the samples in the NIR-treated groups were experimented to be irradiated with an 808 nm laser (1.0 W cm^{-2}, 6 min). NIR light activation showed little impact on the release efficiency of exosomes. By contrast, the DOX release rates of AuNR@DOX-Exos were significantly increased at both pH 5.5 and pH 7.4 upon NIR light activation. After 24 h, ≈50% of the drug had been released in the NIR group, whereas only 35% had been released in the non-NIR group. At pH 7.4, 35% and 20% of the drug had been released in the NIR and non-NIR groups, respectively. This result was attributed to the ability of the AuNR@DOX-Exos to absorb NIR light and transform the energy into heat to destabilize exosome membranes, so as to provide on-demand release of the encapsulated drug.

Figure 2F shows the cytotoxic effects of the AuNRs and AuNR@DOX-Exos with NIR laser irradiation on HeLa cells. The efficiency of cell-killing in terms of the AuNR@DOX-Exos, which was combined with NIR laser irradiation (808 nm, 1.0 W cm^{-2}, 5 min), was significantly higher than that of the AuNRs alone. According to the results above, the improved cytotoxicity of the AuNR@DOX-Exos plus NIR irradiation was supposed to be attributed to the synergistic effects of the photothermal ablation from the AuNRs and chemotherapeutic activity in terms of the DOX that released.

Additionally, we examined whether the heat produced by the NIR laser-irradiated AuNRs attached to the exosome surface
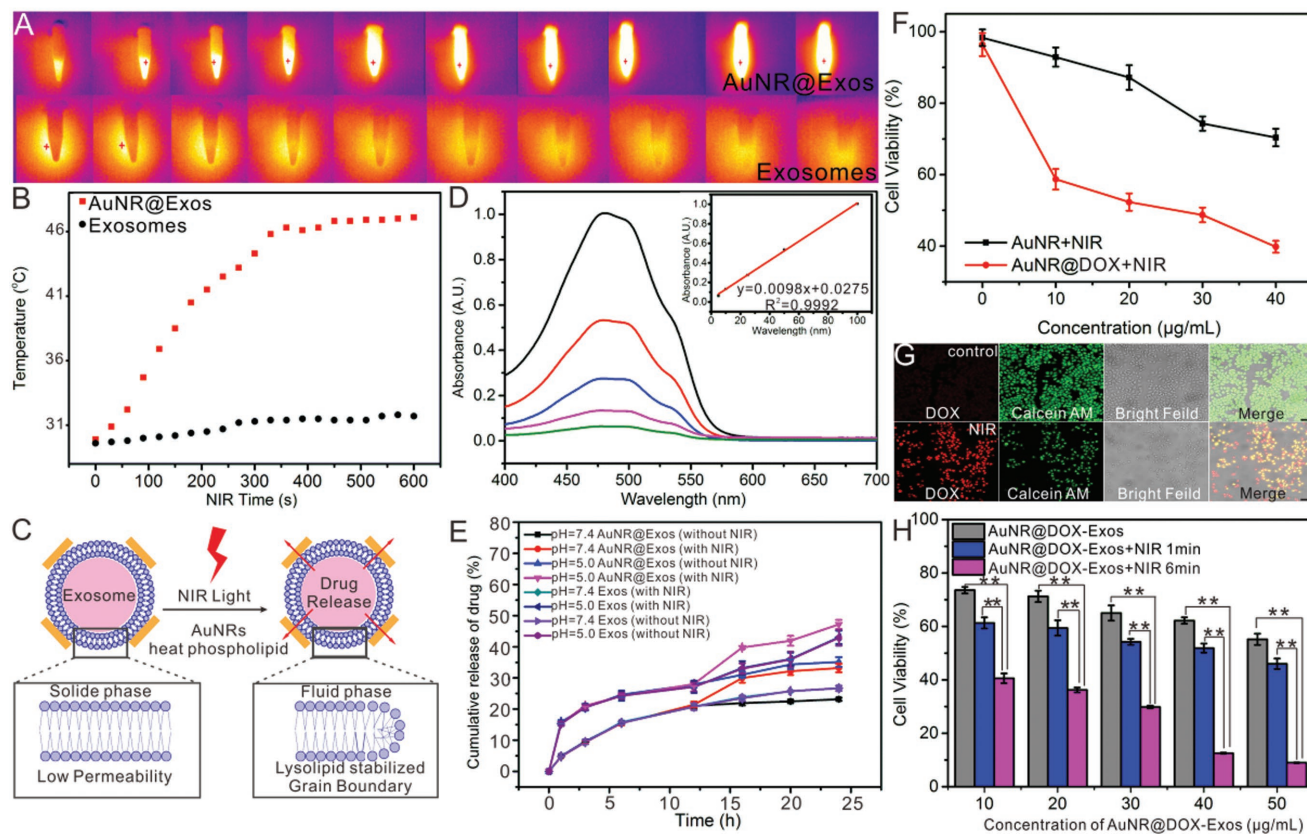
**ADVANCED
SCIENCE NEWS**

www.advancedsciencenews.com

**ADVANCED
FUNCTIONAL
MATERIALS**

www.afm-journal.de

Figure 2. Effect of photothermal conversion by AuNR@Exos. A) IR thermal imaging of an aqueous dispersion of AuNR@Exos (1.0 mg mL^{-1}) with NIR laser irradiation (808 nm, 1.0 W cm^{-2}); the unmodified exosomes were used as a control. B) Photothermal heating curves of AuNR@Exos (1.0 mg mL^{-1}) with NIR laser irradiation (808 nm, 1.0 W cm^{-2}); the unmodified exosomes were used as a control. C) Schematic illustration of drug release from the AuNR@Exos under NIR irradiation. D) UV–vis spectra of DOX at different concentrations. DOX concentrations were calculated according to the standard curve. Data were collected from three independent experiments. E) Drug release profiles of AuNR@Exos and exosomes in vitro at different pH values with or without NIR. All values are expressed as the mean ± SD (n = 3). F) Antitumor effects of the AuNR@DOX-Exos and AuNRs with the NIR laser (808 nm, 1.0 W cm^{-2}, 5 min). Bars correspond to the mean ± SD (n = 3). G) Fluorescence images of HeLa cancer cells treated by incubation with AuNR@DOX-Exos for 4 h with NIR laser irradiation (808 nm, 1.0 W cm^{-2}, 6 min). H) Antitumor effects of the AuNR@DOX-Exos with and without NIR laser irradiation. All values are expressed as the mean ± SD (n = 3). *P < 0.05, **P < 0.01.

could induce the instability of the exosome membrane for effective drug release. The fluorescent images shown in Figure 2G reveal that compared with the nonirradiated cells, the cells irradiated with the laser for 6 min displayed significantly stronger DOX fluorescence signals. In addition, we determined cell viability using the CCK8 assay to directly investigate the in vitro cytotoxicity of the chemo-photothermal therapeutic efficiency of the AuNR@DOX-Exos. It is indicated in Figure 2H that the effect of a concentration-dependent cell-killing could be observed. Furthermore, the antitumor effects were significantly higher with NIR irradiation than without irradiation, with the time of NIR irradiation increased, the viability of cell decreased. Thus, we concluded that the release of DOX from AuNR@DOX-Exos could be boosted by NIR irradiation. Besides, the NIR irradiation can significantly increase cytotoxicity against tumor cells. Importantly, the increased temperature at the irradiated tumor region can easily be adjusted by the spot size and laser power density, enabling controlled drug release on demand.

2.3. Cancer Cell Targeting of FA-AuNR@RGD-Exos In Vitro

To provide further insight into FA-AuNR@RGD-Exos-based targeted therapeutic delivery, we tested the targeting ability of DOX-containing and fluorescein isothiocyanate (FITC) (a green fluorescence emitting dye)-labeled FA-AuNR@RGD-Exos on $\alpha v\beta 3$-negative, FR-negative MCF-7 ($\alpha v\beta 3^-$ and FR$^-$) cells, and $\alpha v\beta 3$-positive, FR-positive HeLa ($\alpha v\beta 3^+$ and FR$^+$) cells. After 4 h of incubation with the FA-AuNR@RGD-DOX-Exos at 37 °C, the HeLa cells showed extensive green fluorescence and red fluorescence, whereas both fluorescent signals were much weaker in the MCF-7 cells, as shown in **Figure 3**A. In addition, green fluorescence in the cytosol of the HeLa cells was evident, as observed from the overlain confocal green fluorescence and bright field images. These results suggested that the FA-AuNR@RGD-Exos selectively accumulated on the cytosol of high $\alpha v\beta 3$-expressing and high FR-expressing cancer cells through receptor-mediated endocytosis and delivered drugs into the cell with high efficiency. The cellular uptake of the FA-AuNR@RGD-Exos was
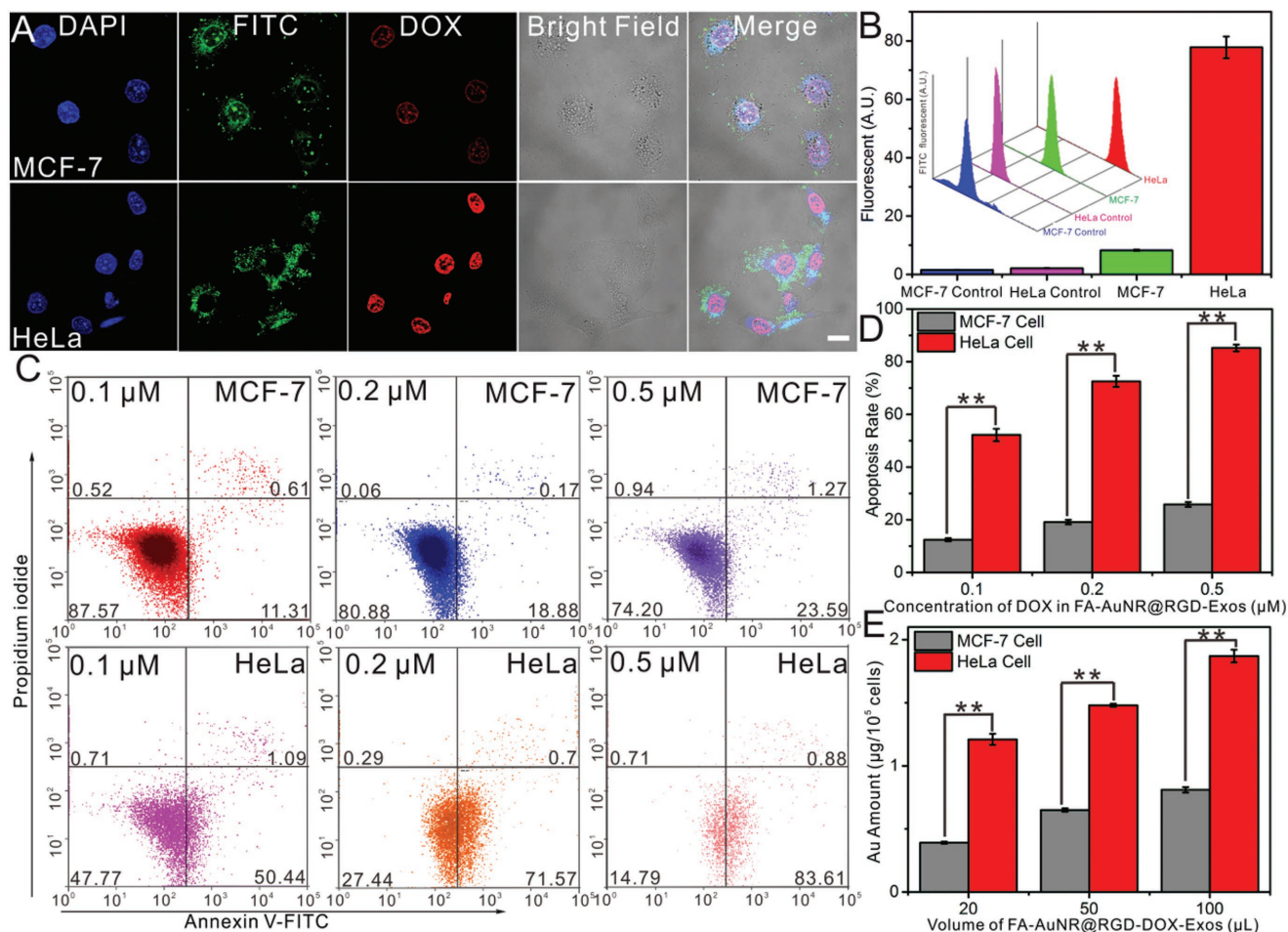
Figure 3. Cancer cell targeting of FA-AuNR@RGD-DOX-Exos in vitro. A) Confocal microscopy images of the cellular uptake of fluorescently labeled FA-AuNR@RGD-DOX-Exos. MCF-7 ($\alpha v \beta 3^-$ and FR$^-$) cells and HeLa ($\alpha v \beta 3^+$ and FR$^+$) cells were treated with fluorescently labeled FA-AuNR@RGD-DOX-Exos for 4 h. Blue color: DAPI-stained cell nuclei. Red color: DOX. Green color: FITC-labeled R-F/P/Au-DOX-Exos. B) Flow cytometric analysis of cancer cell uptake of FA-AuNR@RGD-DOX-Exos after 4 h of incubation. All values are expressed as the mean $\pm$ SD ($n = 3$). C) Flow cytometric analysis of MCF-7 and HeLa cell apoptosis after incubation with different concentrations of FA-AuNR@RGD-DOX-Exos using Annexin V-FITC/PI staining. D) Viability of MCF-7 and HeLa cells after incubation with different concentrations of DOX encapsulated in FA-AuNR@RGD-DOX-Exos. Error bars indicate the SD ($n = 3$). *$P < 0.05$, **$P < 0.01$. E) The amount of Au in the cells treated with different concentrations of FA-AuNR@RGD-DOX-Exos (5 g mL^{-1}) was measured by ICP-MS. Error bars indicate the SD ($n = 3$). *$P < 0.05$, **$P < 0.01$.

analyzed by flow cytometry. HeLa cell ($\alpha v \beta 3^+$ and FR$^+$) uptake of the FA-AuNR@RGD-Exos was nearly 4-fold higher than MCF-7 cell ($\alpha v \beta 3^-$ and FR$^-$) uptake (Figure 3B). Next, we compared the uptake efficiency of different ligand-modified AuNR-functionalized exosomes in HeLa cells. The nuclei of the cells would stain with 4',6-diamidino-2-phenylindole (DAPI) after treating them with FITC-labeled, single or dual ligand modified AuNR@Exos for 12 h (Figure S16, Supporting Information). Compared with the FA-AuNR@Exos-treated and AuNR@RGD-Exos-treated cells, the cytoplasm of the FA-AuNR@RGD-Exos-treated cells exhibited enhanced green fluorescence intensity, showing the synergistic effect of dual ligand functionalization. The results obtained by flow cytometry correlated well with the data collected from confocal images, indicating the fact that the cellular uptake of dual ligand functionalized FA-AuNR@RGD-Exos was nearly 2.5-fold and 7-fold higher than the uptake of single-ligand functionalized FA-AuNR@Exos and AuNR@RGD-Exos,

respectively. Furthermore, we tested the viability of different tumor cells after treatment with different doses of DOX-encapsulated FA-AuNR@RGD-Exos (Figure 3C). The flow cytometry results in Figure 3D show significantly higher apoptosis rates of the HeLa cells than of the MCF-7 cells with different doses of the DOX-encapsulated FA-AuNR@RGD-Exos because of the differential expression of the integrin $\alpha v \beta 3$ and FR receptors. Next, we evaluated the cancer cell targeting ability of the FA-AuNR@RGD-Exos in vitro by measuring cellular uptake of the gold nanoparticles (Figure 3E). Consistent with the fluorescence microscopy and flow cytometry data, the inductively coupled inductively plasma-mass spectrometry (ICP-MS) results demonstrated that the nanocarriers preferably accumulated in the $\alpha v \beta 3^+$ and FR$^+$ cells with different volumes. To assess the target pharmacological effect, we investigated the specificity of FA-AuNR@RGD-Exos for targeting cancer cells (HeLa) over normal cells (NIH-3T3, 293T, and MCF-10A), as shown

**ADVANCED
SCIENCE NEWS**

www.advancedsciencenews.com

**ADVANCED
FUNCTIONAL
MATERIALS**

www.afm-journal.de

in Figure S17 (Supporting Information). The results demonstrated that among the cells tested, the HeLa group exhibited the highest DOX fluorescent intensity, confirming the specific binding of the FA-AuNR@RGD-Exos to cancer cells. In summary, all these data demonstrated that dual ligand functionalization contributed to the highly efficient cancer cell targeting of the exosomes.

2.4. Tumor Targeting of FA-AuNR@RGD-DOX-Exos In Vivo

We used tumor-bearing mouse to characterize the performance of the FA-AuNR@RGD-DOX-Exos in vivo. Cy5.5-labeled, ligand-functionalized FA-AuNR@RGD-DOX-Exos (5 mg mL^{-1}) were then injected intravenously into the tumor-bearing mice and were monitored using a noninvasive near-infrared optical

imaging technique by setting the excitation and emission wavelengths at 675 and 720 nm, respectively.

In the absence of a targeting ligand, only a slight fluorescence signal was observed in the cancer cells (**Figure 4**A). By contrast, for the target ligand-functionalized exosomes, a strong fluorescence signal was detected at the cancer site for 24 h, indicating that the AuNR@Exos decorated with a combination of RGD and FA had a remarkable cancer targeting ability. Compared with the other ligand-functionalized groups, the tumor site of the dual ligand functionalized FA-AuNR@RGD-DOX-Exos showed a higher level of fluorescence and a strong fluorescence signal even at 48 h postinjection, indicating prolonged blood circulation and good tumor targeting ability.

To characterize the tumor targeting effect of various ligand-functionalized AuNR@Exos more accurately, ex vivo fluorescence images of the excised tumor tissues and other major organs were
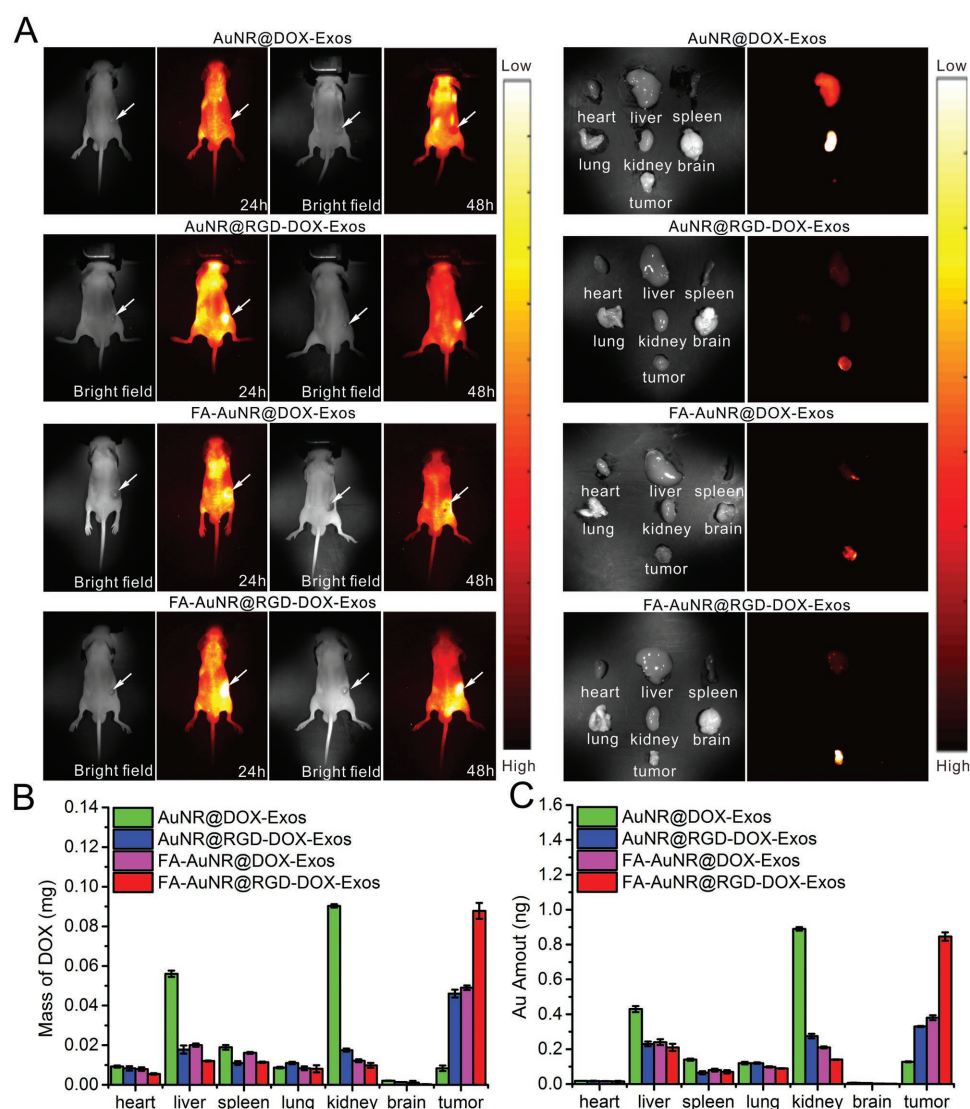

Figure 4. Tumor targeting of functionalized FA-AuNR@RGD-DOX-Exos in HeLa tumor-bearing mice in vivo. A) Left: in vivo NIR fluorescence images of mice injected with single and dual ligand functionalized AuNR@DOX-Exos at the indicated time points after injection. Right: ex vivo fluorescence images of the tumor and other major organs at 48 h postinjection. B) Concentration of DOX in cancer tissue and major organs. Error bars indicate the SD (*n* = 3). C) Concentration of Au in cancer tissue and major organs. Error bars indicate the SD (*n* = 3).

**ADVANCED
SCIENCE NEWS**
www.advancedsciencenews.com

**ADVANCED
FUNCTIONAL
MATERIALS**
www.afm-journal.de

taken after sacrificing the mice at 48 h postinjection. Consistent with the in vivo imaging results, the mice administered the FA-AuNR@RGD-DOX-Exos showed a strong tumor fluorescence signal but nearly no fluorescent signal in the other organs compared with the other three groups. In addition, the distribution of DOX in the major organs and cancer site was tested. As shown in Figure 4B, nonfunctionalized AuNR@Exos changed the DOX biodistribution and accumulated in the tumor through the EPR effect. By contrast, tumors treated with the FA-AuNR@RGD-DOX-Exos exhibited significantly higher signals than any other major organs, whereas liver tissue showed a weak signal. These results revealed that the combination of passive active receptor ligand-mediated targeting of the FA-AuNR@RGD-DOX-Exos provided a higher level of targeting delivery efficiency and increased the DOX concentration. Moreover, the accumulation of Au in the organs and tumor tissues was further measured by ICP-atomic emission spectrometry. As shown in Figure 4C, we found that the Au tumor concentration was the greatest in mice treated with FA-AuNR@RGD-DOX-Exos and was decreased in normal organs in the dual ligand functionalization groups compared with the single ligand or no ligand groups, although the accumulation of ligand-functionalized AuNR@Exos in normal organs was much weaker than that in the tumor. These results verified FA-AuNR@RGD-DOX-Exos as a potential ideal nanomaterial for prolonging circulation, decreasing nonspecific uptake by the liver and targeting tumors with high efficiency.

2.5. Photothermal Efficacy of FA-AuNR@RGD-Exos In Vivo

The excellent in vivo tumor targeting effect of the FA-AuNR@RGD-Exos encouraged us to investigate its photothermal therapeutic efficacy on tumor xenograft mice. The time-dependent biodistribution of NIR signals was captured by the intravital fluorescence imaging system. As shown in **Figure 5**A, during

the 48 h postinjection, in the tumor site, the strong fluorescence (Cy5.5) intensity of the FA-AuNR@RGD-Exos indicating the fact that FA-AuNR@RGD-Exos showed better tumor targeting efficacy.

At the time-point of 48 h of the postinjection, the tumors were experimented to expose to NIR laser irradiation in terms of photothermal treatment. At the tumor site, the temperature increased after the mice treated with FA-AuNR@RGD-Exos upon the NIR laser irradiation (808 nm, 1.0 W cm^{-2}, 6 min), as monitored by an IR thermal camera (Figure 5B), was from 36.1 to 47.5 °C, which could enhance drug release and effect irreversible tumor tissue damage. By contrast, the same laser irradiation of tumors injected with saline yielded a maximal temperature below 38.2 °C, which would be ineffective at irreversibly damaging tumor tissues (Figure 5C).

After the mice treated with NIR laser irradiation were sacrificed, ex vivo fluorescence images of the excised tumor tissues and other major organs were taken (Figure 5D). Notably, nearly all the FA-AuNR@RGD-Exos accumulated at the tumor site. This excellent targeting ability of the FA-AuNR@RGD-Exos probably resulted from the unique physicochemical properties and excellent biocompatibility of the exosomes. Importantly, the photothermal ability of the NIR laser-irradiated FA-AuNR@RGD-Exos had no impact on their tumor targeting efficacy.

2.6. Synergistic Photothermal Chemotherapy Effects of FA-AuNR@RGD-DOX-Exos In Vivo

Mice bearing HeLa cells received intravenous injections of saline (200 µL) (G1), FA-AuNR (5 mg mL^{-1}, 200 µL) (G2), FA-AuNR@RGD-Exos (5 mg mL^{-1}, 200 µL) (G3), FA-AuNR@DOX-Exos (5 mg mL^{-1}, 200 µL) (G4), or FA-AuNR@RGD-DOX-Exos (5 mg mL^{-1}, 200 µL) (G5). Tumors were treated with the NIR laser (808 nm, 1.0 W cm^{-2}) for 6 min at 2, 4, 6, 8, and 10 d postinjection. As shown in **Figure 6**A,B, the saline plus
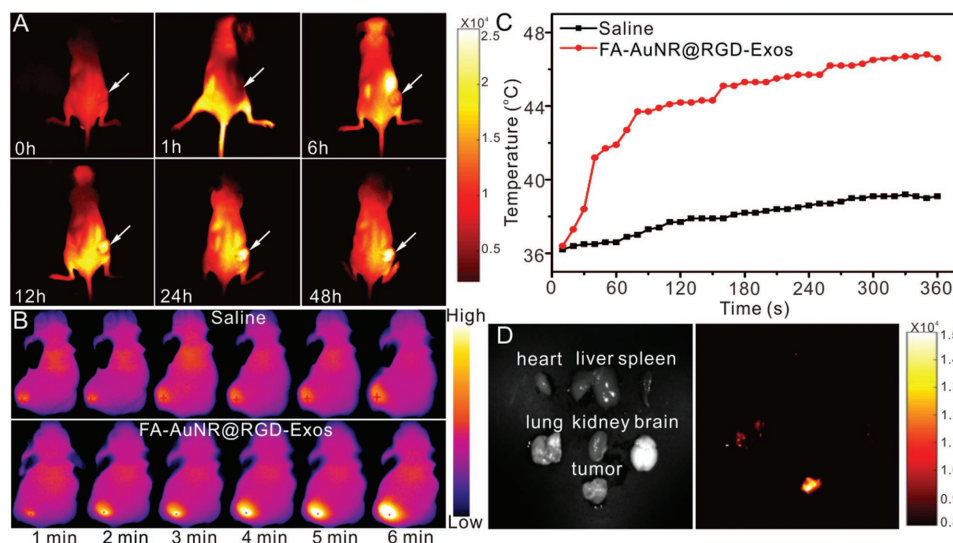

Figure 5. A) Overall fluorescence imaging of HeLa xenograft nude mice after the injection of FA-AuNR@RGD-DOX-Exos. In vivo NIR fluorescence images were taken before injection and at 1, 6, 12, 24, and 48 h postinjection. B) Thermal imaging and C) photothermal heating curves of FA-AuNR@RGD-DOX-Exos in mice tumors irradiated with an 808 nm laser (1.0 W cm^{-2}, 10 min). D) Ex vivo fluorescence images of the tumor and other major organs at 48 h postinjection.
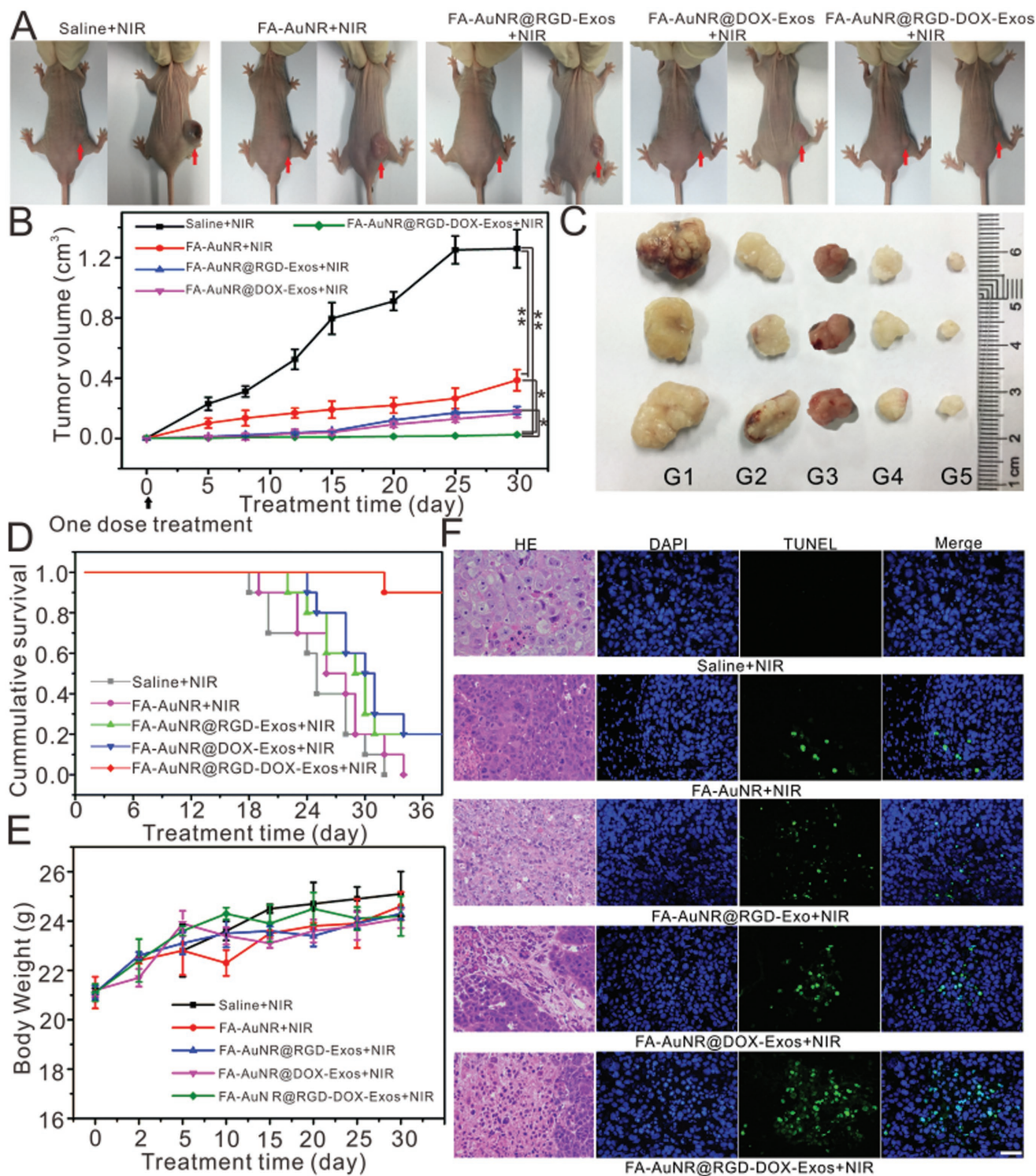
Figure 6. A) Representative images of the xenograft tumors in mice after treatment with different nanocarriers (saline, FA-AuNR, FA-AuNR@DOX-Exos, FA-AuNR@RGD-Exos, and FA-AuNR@RGD-DOX-Exos) and NIR irradiation at day 4 (left) and day 15 (right). B) Tumor growth curves after intravenous injection of the different nanocarriers under NIR irradiation. One dose was administered at day 0. Error bars indicate the SD ($n = 8$). $*P < 0.05$, $**P < 0.01$. C) Images of typical tumors at the end of the experiment. D) The cumulative survival of tumor-bearing nude mice after intravenous injection of different nanocarriers. Error bars indicate the SD ($n = 8$). E) Body weight changes in the mice after treatment. Error bars indicate the SD ($n = 8$). F) TUNEL staining of tumor sections from the mice injected with 200 µL of different nanocarriers (saline, FA-AuNR, FA-AuNR@RGD-Exos, FA-AuNR@DOX-Exos, and FA-AuNR@RGD-DOX-Exos) (5.0 mg mL^{-1}) and treated with NIR irradiation (808 nm laser, 1.0 W cm^{-2}, 6 min). Scale bar = 200 µm for all images.

NIR laser group mice exhibited rapid tumor growth from 0 to 5 d postinjection, demonstrating the fact that laser irradiation did not influence the tumor growth. The FA-AuNR + laser group showed apparent efficacy in restricting tumor growth because FA mediated the AuNR tumor accumulation and because the NIR light absorbed by the AuNRs was converted into cytotoxic heat, thus destroying hyperthermia-sensitive tumor cells. By contrast, mice treated with FA-AuNR@RGD-Exos + NIR laser, FA-AuNR@DOX-Exos + NIR laser, and FA-AuNR@RGD-DOX-Exos + NIR laser exhibited significant tumor growth inhibition, which resulted from the tumor cell death mediated by the localized hyperthermia induced by the AuNRs and by the heat-enhanced encapsulated drug release from the exosomes. Notably, Both FA-AuNR@RGD-Exos + NIR laser and FA-AuNR@DOX-Exos + NIR laser could inhibit tumor growth within only the first 15 d, after which the tumors eventually recurred. By contrast FA-AuNR@RGD-DOX-Exos + NIR laser could inhibit tumor growth for 30 d because of the synergistic targeting effect of the FA and RGD dual ligands on tumors and the higher tumor accumulation of the nanocarriers via receptor-mediated cellular uptake.

The images in Figure 6C were typical tumors which were collected at the end of the treatment period, providing insight into the antitumor efficacy of the different treatments. Among the treatment groups, the tumor size of the FA-AuNR@RGD-DOX-Exos with NIR irradiation group was the smallest, confirming that the FA-AuNR@RGD-DOX-Exos was capable of effective chemo-photothermal antitumor treatment. For the purpose to assess the survival time of the experimented mice, analysis of the Kaplan–Meier with log-rank test was conducted, of which the results were shown in Figure 6D. No animal survived longer than 28 d in the group of saline combined with NIR laser, whereas the animal survival time in the FA-AuNR@RGD-Exos + NIR laser group and FA-AuNR@DOX-Exos + NIR laser group was prolonged and was improved compared with the FA-AuNR + NIR laser group. Importantly, the FA-AuNR@RGD-DOX-Exos + NIR laser group showed the best efficiency at tumor growth inhibition and showed the longest survival time. As there exist no obvious variations in mice weight in any of the treated groups, the experimental treatments were well tolerated (Figure 6E). Furthermore, in the tumor tissues, we evaluated apoptosis by using TUNEL, which represents the terminal deoxynucleotidyl transferase dUTP nick end labeling assay, as well as H&E (hematoxylin and eosin) staining. As shown in Figure 6F, among the treatment groups, the highest cell apoptosis rate, as well as substantial cell remission, occurred in the tumors treated with FA-AuNR@RGD-DOX-Exos under NIR irradiation, further confirming the synergistic effect of dual ligand mediated targeted photothermal chemotherapy on suppressing tumor growth.

For the purpose of evaluating the biosafety of FA-AuNR@RGD-DOX-Exos in vivo, FA-AuNR@RGD-DOX-Exos (5 mg mL^{-1}, 200 µL) were injected into the tail vein of BALB/c mice. The toxicity of FA-AuNR@RGD-DOX-Exos to major organs was investigated by H&E staining, hematological analysis, and liver/kidney function indices (liver functions indices: alanine aminotransferase (ALT) and aspartate aminotransferase (AST); kidney function indices: creatinine (CRE) and blood urea nitrogen (BUN)), as determined by a blood biochemistry test. As shown in Figure S18 (Supporting Information), apparent organ injury and inflammation changes were not observed in the FA-AuNR@RGD-DOX-Exos group compared with those in the control group, indicating the negligible histological toxicity and biocompatibility and biosafety of treatment with FA-AuNR@RGD-DOX-Exos in mice. The results from hematological analysis showed that indicators for blood cells, hemoglobin, and platelets did not significantly change, even after 3 weeks (Figure S19, Supporting Information). Moreover, the ALT/AST/CRE/BUN concentration showed no obvious changes compared with the control group (Figure S20, Supporting Information). Although the quantitative result (Figure S21, Supporting Information) obtained by fluorescence activated cell sorting showed that our engineered exosomes had more opportunity to be engulfed by phagocytes cell than pure exosomes, it showed superior tumor targeting ability than unmodified ones (Figure S22, Supporting Information). These results demonstrated that our proposed FA-AuNR@RGD-DOX-Exo is a biocompatible nanocarrier without significant side effects in vivo. The excellent synergistic photothermal chemotherapy efficacy of the biocompatible engineered exosomes inspired us to develop natural theranostic nanoplatforms, which are promising tools for clinical treatment.

3. Conclusion

In summary, exosomes have shown advantages as drug delivery platform. It not only can efficiently transport drug between cells but also can overcome various biological barriers. However, there still remain several challenges before exosomes used at clinical applications, including the development of exosomes capable of efficient targeted drug delivery and controlled drug release. To date, there is no report about a method for simultaneously achieving active targeting and stimuli-responsive controlled release of engineered exosomes to enhance therapy efficacy and reduce side effects. Most promisingly, we developed a platform for targeted combined tumor chemo-photothermal therapy based on dual ligand functionalized, AuNR-conjugated exosomes (FA-AuNR@RGD-Exos) by a biofriendly and convenient donor-cell assisted strategy. The engineered exosomes could accumulate at the tumor site with high efficiency because of the cooperative dual ligand targeting through receptor-mediated endocytosis. The AuNRs attached to the exosomes could transform NIR light into heat with high efficiency. Moreover, the heat could impact the permeability of exosomes membrane by affecting the lipid bilayer and/or transmembrane proteins to enhance drug release from the carriers. Notably, this NIR-enhanced drug release on-demand behavior could be rapidly, selectively, and locally activated by remote controlling the NIR laser parameters, including the spot size and laser power density. Consequently, FA-AuNR@RGD-Exos showed an outstanding chemo-photothermal synergistic therapeutic effect both in vitro and in vivo. It served as a novel platform for developing new "biotech drugs" with excellent therapeutic efficiency and targeting capacity for precise cancer therapy.

4. Experimental Section

Materials and Reagents: All culture consumables for cell culture were purchased from Corning (Acton, MA). All culture media, FBS,

**ADVANCED
SCIENCE NEWS**

www.advancedsciencenews.com

**ADVANCED
FUNCTIONAL
MATERIALS**

www.afm-journal.de

and phosphate-buffered saline (PBS) buffer were bought from Gibco Life Technologies Corporation (Grand Island, NY, USA). DAPI, calcein acetoxymethyl ester (Calcein-AM), propidium iodide (PI), DOX, phorbol-12-myristate-12-acetate (PMA), sodium hydroxide (NaOH), FA, HS-poly (ethylene glycol) (PEG)-NH$_2$ were bought from Sigma-Aldrich (St. Louis, MO, USA). CCK-8 kit was purchased from Thermo Scientific (Waltham, MA, USA). Commercially available AuNR with peak absorption in the near infrared was purchased from NANOEAST Biotech (Nanjing, China). RGD functionalized 1,2-dioleoyl-sn-glycero-3-phosphoethanolamine-poly (ethylene glycol)-2000 (DSPE-PEG-RGD), sulfhydryl functionalized 1,2-dioleoyl-sn-glycero-3-phosphoethanolamine-poly (ethylene glycol)-2000 (DSPE-PEG-SH), and NHS-FA were purchased from Ponsure Biotech (Shanghai, China). Flow-count calibrator beads were purchased from Beckman Coulter (Miami, FL, USA). Fluorochrome-labeled antibodies for flow cytometry including CD63-TRITC and CD81-FITC, Mouse anti-FA monoclonal antibody, and Mouse anti-RGD monoclonal antibody were bought from BD Biosciences located in San Diego, CA, USA. With the aim to prepare for all solutions, a Millipore-Q system was put into use to purify the water. All the chemicals involved were of analytical grade.

Cell Culture: The human THP-1 cells were bought from the American Type Culture Collection (ATCC, Manassas, VA). Supplemented with 10% (v/v) FBS 1% (v/v) and antibiotic, the RPMI 1640 medium was used to maintain the THP-1 cells. It is requested that the cell cultures were supposed to be incubated in a circumstance at 37 °C in a 95% air/5% CO$_2$ atmosphere.

Preparation of AuNR@RGD-DOX-Exos: THP-1 cells were induced into macrophages via incubated with 320×10^{-9} M PMA for 12 h. To achieve the macrophages modified with RGD and sulfhydryl, macrophages were cultured in RPMI 1640 medium containing 10% exosome-depleted FBS, DSPE-PEG-SH (0–50 µg mL^{-1}), and DSPE-PEG-RGD (0–5 µg mL^{-1}, 1/10 of DSPE-PEG-SH). It was maintained routinely under normal conditions for 3 d. Under the condition at $150\,000 \times g$ for 16 h at 4 °C, ultracentrifugation was used to collect Exosome-depleted FBS. The engineered exosomes were purified from the supernatants of starved macrophages cells according to the method as previously report.[34] Besides, serial centrifugation was put into use to remove cells and debris for 10 min at $500 \times g$ and for 20 min $3000 \times g$ at 4 °C. Ultracentrifugation at $150\,000 \times g$ for 2 h at 4 °C was being used to isolate the engineered exosomes. Furthermore, to analyze the engineered exosomes membrane markers, standard microbeads with a diameter of 300 nm were used to set the upper size limit of the exosomes, and this population was used to gate the exosomes. The engineered exosomes were stained with anti-CD63 antibody and anti-CD81 antibody. We used a FAC Scan flow cytometer (Becton Dickinson, San Diego, CA, USA) to analyse flow cytometry experiment result.

To load DOX into the engineered exosomes, the engineered exosomes (2 mg mL^{-1}, 50 µL) and DOX were mixed in 250 µL electroporation buffers in 0.4 cm cuvette (Bio-Rad). Electroporation was then carried out at 250 V and 350 µF on a Bio-Rad Gene Pulser Xcell Electroporation System. After electroporation, the mixture was incubated at 37 °C for 30 min to allow the recovery of the membrane of the electroporated exosomes. AuNR (5.0×10^{-9} M) and the engineered exosomes (2 mg mL^{-1}) were reacted at shaking incubator at room temperature for 20 h for the purpose to form AuNR@RGD-DOX-Exos.

Characterization: For TEM characterization, purified exosomes, RGD-Exos-SH, FA-AuNR@RGD-Exos solutions were dropped onto a carbon-coated copper grid and stained with 2% uranyl acetate. The transmission electron microscope was used at 75 kV to observe samples (8H-7000FA, Hitachi, Japan). Nano-ZEN 3600 (Malvern Instruments, UK) was used to test the hydrodynamic diameters and zeta potential of suspended purified exosomes, RGD-Exos-SH and FA-AuNR@RGD-Exos. And the spectrophotometer (UV2550, Shimadzu, Japan) was used to test the UV–vis absorption spectra. With the speed of 2 mm s^{-1} by an FTIR spectrometer, in the range of 400–4000 cm^{-1}, FTIR analyses in terms of pure exosomes and FA-AuNR@RGD-Exos as well as RGD-Exos-SH were recorded (VERTEX 70, Bruker, Germany).

Preparations of FA-AuNR@RGD-Exos: AuNR@RGD-Exos was resuspended in 100 µL of PBS buffer and then HS-PEG-NH$_2$

(10×10^{-6} M, 100 µL) was added into the AuNR@RGD-Exos solution, and then in a dark circumstance at room temperature, it was stirred for 4 h. After centrifuging the reaction solution at 9000 g for 5 min at the temperature of 25 °C, the obtained precipitate was washed twice for the purpose of removing the excess HS-PEG-NH$_2$. After that, 20 µL of NHS-FA (0.1 M, in dimethyl sulfoxide) at PBS (pH = 11) was reacted with the functionalized AuNR@RGD-Exos solution of 1.0 mL for 8 h. In order to obtain the precipitates, ultracentrifugation was used to collect the mixture for 5 min at 9000 g. The precipitates were washed twice using PBS and resuspended in PBS for further use.

Stability Study: In terms of the effect of therapy, the stability of nanocarrier for drug delivery plays an important role. During the study, after different periods in various days, the stability of FA-AuNR@RGD-DOX-Exos was tested under the condition that it was after the storage at 4, 25, and 37 °C, respectively. On different days at certain time-points, the FA-AuNR@RGD-DOX-Exos' stability was evaluated by hydrodynamic diameters.

Drug Release Assay: Under the circumstances of pH 5.5 and pH 7.4, respectively, by using a dynamic dialysis method, the released performances of DOX from FA-AuNR@RGD-DOX-Exos were demonstrated. For the purpose of simulating the normal environments of body and the tumor, the PBS media of pH 7.4 and pH 5.5 were put into use. Further, they were separated into 2 groups, which are non-NIR groups and NIR group. Loaded in the dialysis bag (cutoff = 14 kDa), sample (4 mL) was then immersed in 100 mL of PBS and it was stirred with 100 rpm at the temperature of 37 °C. At some predetermined time-points including 12, 16, 20, and 24 h, in the NIR groups, the samples were irradiated with NIR light (808 nm, 1.0 W cm^{-2}) for 6 min. Concentration of DOX was determined by UV–vis absorption spectroscopy and all tests were taken in triplicates.

Cancer Cell Targeting Confocal Imaging Study In Vitro: FITC signals of FA-AuNR@RGD-DOX-Exos uptake rates of different cancer cells were detected. Confocal fluorescence microscopy was used to assess intracellular trafficking of FA-AuNR@RGD-DOX-Exos. Cells grown on glass coverslips (pretreated with polylysine) of a six-well plate were incubated with FITC-labeled FA-AuNR@RGD-DOX-Exos for 4 h. Following incubation, the cells were washed three times with PBS and were fixed in paraformaldehyde for 15 min. Cells were stained with DAPI fluorescent dye. Localization of FITC labeled FA-AuNR@RGD-DOX-Exos and DOX in cells was visualized using a confocal microscope ((FV 1000, Olympus, Japan) with identical settings. FITC signal uptake rates were detected using flow cytometry. According to the above method, the same concentrations (50 µg mL^{-1}) of FITC labeled different ligand modified AuNR@Exos (FA-AuNR@Exos, AuNR@RGD-Exos, FA-AuNR@RGD-Exos) were added to the HeLa cells and incubated for 12 h at 37 °C. Samples were visualized using a confocal microscope and the uptake efficiency was detected using flow cytometry.

Cellular Uptake Flow Cytometry Study In Vitro: Flow cytometry was used for quantitative analysis of cell uptake. HeLa cells and nontumor cells (NIH-3T3, 293T, MCF-10A) were seeded in12-well plate (4×10^5 cells mL^{-1}) and cultured for 12 h. Cells were changed with a medium containing 50 µg mL^{-1} of FA-AuNR@RGD-DOX-Exos. Cells were washed three times using PBS and were then harvested, and the fluorescence histograms of DOX were recorded by flow cytometer (FC500, Beckman Coulter).

Cell Viability Assay: The cytotoxicity of FA-AuNR@RGD-DOX-Exos in cancer cells was evaluated using a CCK-8 kit. First, HeLa cells (4×10^5 cells mL^{-1}, 100 µL per well) were seeded into 96-well plates and grown in complete dulbecco's modified eagle medium (DMEM) containing 10% (v/v) FBS at 37 °C for 24 h. Subsequently, the culture medium in each well was replaced with PBS and added with fresh complete medium DMEM medium containing 10% (v/v) exosome-depleted FBS that contained different concentrations of FA-AuNR@RGD-DOX-Exos. Cells added with PBS in wells were used as a control group. Every group was treated with NIR light irradiation or without it, for the purpose to make a comparison. FA-AuNR@RGD-DOX-Exos were filtered via the filter membrane of sterile 0.22 µm and then were diluted to different concentrations (10, 20, 30, 40, 50 µg mL^{-1}) and were added

to the HeLa cells (4×10^5 cells mL^{-1}, 100 µL per well). After incubation of 4 h, the NIR groups were then exposed to NIR light (808 nm, 1.0 W cm^{-2}) condition for different time and incubated for 20 h continuously. By comparison, the other groups were directly incubated with the samples for 24 h. After the treatment above, CCK-8 solution (10 µL) was added and its absorbance was measured at 450 nm to calculate the viability of cells (Synergy, Bio-Tek, USA).

Establishment of Xenografts in Nude Mice: HeLa cells (10^8 cells in 100 µL medium) were inoculated subcutaneously into the flanks of the male nude mice (18–20 g, 4 weeks old) to establish cervical cancer-bearing mouse model. The tumor growth was assessed by measuring the size of the xenografts every two days, and the tumor volumes were calculated according to the formula as Volume = (Length $\times$ Width^2)/2.

Tumor Targeting Study In Vivo: The engineered exosomes were labeled by NHS-Cy5.5 (mass ratio of 100:1) in pH 8.5 buffer solution for 4 h. When the tumor volumes reached to 50 mm^3, the tumor-bearing mice were weighed and randomly divided into four groups ($n = 8$) and injected intravenously with different solutions: AuNR@DOX-Exos, AuNR@RGD-DOX-Exos, FA-AuNR@DOX-Exos, FA-AuNR@RGD-DOX-Exos (5 mg mL^{-1}, 200 µL per mice), whereas the control group was injected with saline. After injection for 1, 6, 12, 24, and 48 h, nude mice were imaged using the CRI Maestro in vivo fluorescence imaging system. After 48 h, the mice were euthanized, and major organs were harvested. All experimental protocols were conducted within Huazhong University of Science and Technology's guidelines for animal research and were approved by the Institutional Animal Care and Use Committee. The tumors were stored overnight in 4.0% (v/v) paraformaldehyde solution and were then washed twice with PBS to remove excess formaldehyde. Paraffin embedded tissue sections and dissected into sections (7 µm) were then stained with hematoxylin and eosin (H&E) and observed through an optical microscope (Olympus IX51, Japan). For the TUNEL apoptosis staining, the fixed tumor sections were stained by 50 µL TUNEL reaction mixture (Roche) for 60 min at 37 °C according to the manufacturer's protocol. The cell nuclei were visualized by staining with DAPI. Images were captured using an inverted fluorescence microscope (IX71, Olympus, Japan). The amount of Au on the liposomal surface was measured by ionizing the sample with ICP spectroscopy (ELAN DRC-e, PerkinElmer, USA) followed by MS to separate and quantify the generated ions.

Photothermal Effect of the FA-AuNR@RGD-DOX-Exos on Solid Tumors: The photothermal conversion effect of FA-AuNR@RGD-DOX-Exos was also evaluated in tumor mice. Two mice bearing HeLa tumors were injected (tail vein intravenous injection) with saline (200 µL) or FA-AuNR@RGD-DOX-Exos (200 µL, 5 mg mL^{-1}). After 48 h, the tumors were irradiated with an 808 nm NIR laser (1.0 W cm^{-2}, 6 min). The thermal imaging and temperature increase were monitored by using a photothermal imaging system (PI400, Optris, Germany).

Chemo-Photothermal Synergistic Therapy of Cancer In Vivo by FA-AuNR@RGD-DOX-Exos: To measure the chemo-photothermal synergistic therapy effect of cancer, the HeLa tumor-bearing mice were randomly separated into four groups (three mice in each group) and intravenously injected (tail vein intravenous injection) with saline (200 µL) (G1), FA-AuNR (5 mg mL^{-1}, 200 µL) (G2), FA-AuNR@RGD-Exos (5 mg mL^{-1}, 200 µL) (G3), FA-AuNR@DOX-Exos (5 mg mL^{-1}, 200 µL) (G4), and FA-AuNR@RGD-DOX-Exos (5 mg mL^{-1}, 200 µL) (G5). At 24 h postinjection, the NIR laser (808 nm, 1.0 W cm^{-2}) was used to irradiate the tumors for 6 min. The changes in the tumor volume and body weight were monitored, and according to the animal protocol, the experimented mice of tumor sizes exceeding 2000 m^3 were euthanized.

Biosafety of FA-AuNR@RGD-DOX-Exos In Vivo: The male BALB/c mice (5 per group) were intravenous injected via the tail vein with PBS, Exosomes, and FA-AuNR@RGD-DOX-Exos (200 µL, 5 mg mL^{-1}, $n = 5$). The mice were euthanized after three weeks and ≈600 µL blood samples were collected from each mouse, followed by blood chemistry tests and whole blood cell analyses. The ALT/AST and BUN/CRE were evaluated by a liver and renal function activity assay kit (JianCheng Biotech, China). Major organs were excised, fixed in 4% buffered paraformaldehyde for 24 h, then embedded, sliced into 6 µm sections for H&E staining, which was observed using an Olympus microscope (Olympus IX51, Japan).

Statistical Analysis: The quantitative data were analyzed by Student's t-test. P value is expressed as the differences between control and experimental samples. The difference of $**P < 0.01$ is more significant than $*P < 0.05$.

Supporting Information

Supporting Information is available from the Wiley Online Library or from the author.

Conflict of Interest

The authors declare no conflict of interest.

[1] a) C. D. Kaddi, J. H. Phan, M. D. Wang, *Nanomedicine* **2013**, *8*, 1323; b) L. Lartigue, C. Innocenti, T. Kalaivani, A. Awwad, M. d. M. S. Duque, Y. Guari, J. Larionova, C. Guerin, J.-L. G. Montero, V. Barragan-Montero, P. Arosio, A. Lascialfari, D. Gatteschi, C. Sangregorio, *J. Am. Chem. Soc.* **2011**, *133*, 10459; c) R. S. McCoy, S. Choi, G. Collins, B. J. Ackerson, C. J. Ackerson, *ACS Nano* **2013**, *7*, 2610; d) D. Pissuwan, S. M. Valenzuela, C. M. Miller, M. C. Killingsworth, M. B. Cortie, *Small* **2009**, *5*, 1030.

[2] a) N. Lewinski, V. Colvin, R. Drezek, *Small* **2008**, *4*, 26; b) A. S. Barnard, *Nat. Mater.* **2006**, *5*, 245.

[3] a) M. Liong, J. Lu, M. Kovochich, T. Xia, S. G. Ruehm, A. E. Nel, F. Tamanoi, J. I. Zink, *ACS Nano* **2008**, *2*, 889; b) S. Mura, J. Nicolas, P. Couvreur, *Nat. Mater.* **2013**, *12*, 991; c) S. Rani, T. Ritter, *Adv. Mater.* **2016**, *28*, 5542.

[4] a) L. Feng, M. Gao, D. Tao, Q. Chen, H. Wang, Z. Dong, M. Chen, Z. Liu, *Adv. Funct. Mater.* **2016**, *26*, 2207; b) M. Li, C. Teh, C. Y. Ang, S. Y. Tan, Z. Luo, Q. Qu, Y. Zhang, V. Korzh, Y. Zhao, *Adv. Funct. Mater.* **2015**, *25*, 5602; c) S. Li, B. Goins, L. Zhang, A. Bao, *Bioconjugate Chem.* **2012**, *23*, 1322; d) D. Luo, K. A. Carter, A. Razi, J. Geng, S. Shao, D. Giraldo, U. Sunar, J. Ortega, J. F. Lovell, *Biomaterials* **2016**, *75*, 193; e) A. K. Rengan, A. B. Bukhari, A. Pradhan, R. Malhotra, R. Banerjee, R. Srivastava, A. De, *Nano Lett.* **2015**, *15*, 842; f) A. Schaedlich, H. Caysa, T. Mueller, F. Tenambergen, C. Rose, A. Goepferich, J. Kuntsche, K. Maeder, *ACS Nano* **2011**, *5*, 8710; g) D. V. Volodkin, A. G. Skirtach, H. Moehwald, *Angew. Chem., Int. Ed.* **2009**, *48*, 1807; h) J. Wang, J. Liu, Y. Liu, L. Wang, M. Cao, Y. Ji, X. Wu, Y. Xu, B. Bai, Q. Miao, C. Chen, Y. Zhao, *Adv.*

ADVANCED
SCIENCE NEWS

www.advancedsciencenews.com

ADVANCED
FUNCTIONAL
MATERIALS

www.afm-journal.de

Mater. **2016**, *28*, 8950; i) G. Wu, A. Milkhailovsky, H. A. Khant, C. Fu, W. Chiu, J. A. Zasadzinski, *J. Am. Chem. Soc.* **2008**, *130*, 8175; j) C. Yao, P. Wang, X. Li, X. Hu, J. Hou, L. Wang, F. Zhang, *Adv. Mater.* **2016**, *28*, 9341; k) T. Zheng, G. G. Li, F. Zhou, R. Wu, J.-J. Zhu, H. Wang, *Adv. Mater.* **2016**, *28*, 8218.

[5] a) G. Raposo, W. Stoorvogel, *J. Cell Biol.* **2013**, *200*, 373; b) C. Thery, L. Zitvogel, S. Amigorena, *Nat. Rev. Immunol.* **2002**, *2*, 569.

[6] Y. Yang, Y. Hong, G. H. Nam, J. H. Chung, E. Koh, I. S. Kim, *Adv. Mater.* **2017**, *29*, 1605604.

[7] a) J. Skog, T. Wuerdinger, S. van Rijn, D. H. Meijer, L. Gainche, M. Sena-Esteves, W. T. Curry Jr., B. S. Carter, A. M. Krichevsky, X. O. Breakefield, *Nat. Cell Biol.* **2008**, *10*, 1470; b) C. Thery, M. Ostrowski, E. Segura, *Nat. Rev. Immunol.* **2009**, *9*, 581; c) H. Valadi, K. Ekstrom, A. Bossios, M. Sjostrand, J. J. Lee, J. O. Lotvall, *Nat. Cell Biol.* **2007**, *9*, 654.

[8] L. Alvarez-Erviti, Y. Seow, H. Yin, C. Betts, S. Lakhal, M. J. A. Wood, *Nat. Biotechnol.* **2011**, *29*, 341.

[9] a) S. C. Jang, O. Y. Kim, C. M. Yoon, D.-S. Choi, T.-Y. Roh, J. Park, J. Nilsson, J. Lotvall, Y.-K. Kim, Y. S. Gho, *ACS Nano* **2013**, *7*, 7698; b) Y. Tian, S. Li, J. Song, T. Ji, M. Zhu, G. J. Anderson, J. Wei, G. Nie, *Biomaterials* **2014**, *35*, 2383; c) J. G. van den Boorn, M. Schlee, C. Coch, G. Hartmann, *Nat. Biotechnol.* **2011**, *29*, 325.

[10] S. El Andaloussi, S. Lakhal, I. Maeger, M. J. A. Wood, *Adv. Drug Delivery Rev.* **2013**, *65*, 391.

[11] a) M. J. Haney, N. L. Klyachko, Y. Zhaoa, R. Gupta, E. G. Plotnikova, Z. He, T. Patel, A. Piroyan, M. Sokolsky, A. V. Kabanov, E. V. Batrakova, *J. Controlled Release* **2015**, *207*, 18; b) A. Kalani, A. Tyagi, N. Tyagi, *Mol. Neurobiol.* **2014**, *49*, 590.

[12] S. E. Headland, H. R. Jones, L. V. Norling, A. Kim, P. R. Souza, E. Corsiero, C. D. Gil, A. Nerviani, F. Dell'Accio, C. Pitzalis, S. M. Oliani, L. Y. Jan, M. Perretti, *Sci. Transl. Med.* **2015**, *7*, 315ra190.

[13] K. B. Johnsen, J. M. Gudbergsson, M. N. Skov, L. Pilgaard, T. Moos, M. Duroux, *Biochim. Biophys. Acta, Rev. Cancer* **2014**, *1846*, 75.

[14] a) S.-I. Ohno, M. Takanashi, K. Sudo, S. Ueda, A. Ishikawa, N. Matsuyama, K. Fujita, T. Mizutani, T. Ohgi, T. Ochiya, N. Gotoh, M. Kuroda, *Mol. Ther.* **2013**, *21*, 185; b) Y. Jin, J. S. Lee, S. Min, H.-J. Park, T. J. Kang, S.-W. Cho, *Adv. Funct. Mater.* **2016**, *26*, 5804.

[15] H. Qi, C. Liu, L. Long, Y. Ren, S. Zhang, X. Chang, X. Qian, H. Jia, J. Zhao, J. Sun, X. Hou, X. Yuan, C. Kang, *ACS Nano* **2016**, *10*, 3323.

[16] J. Gautier, E. Allard-Vannier, E. Munnier, M. Souce, I. Chourpa, *J. Controlled Release* **2013**, *169*, 48.

[17] A. Sadana, T. Vo-Dinh, *Appl. Biochem. Biotechnol.* **1997**, *67*, 1.

[18] P. Zhang, C. Wang, J. Zhao, A. Xiao, Q. Shen, L. Li, J. Li, J. Zhang, Q. Min, J. Chen, H.-Y. Chen, J.-J. Zhu, *ACS Nano* **2016**, *10*, 3637.

[19] K. C. Hribar, M. H. Lee, D. Lee, J. A. Burdick, *ACS Nano* **2011**, *5*, 2948.

[20] T. Yamamoto, Y. Teramura, T. Itagaki, Y. Arima, H. Iwata, *Sci. Technol. Adv. Mater.* **2016**, *17*, 677.

[21] a) J. Wang, W. Li, L. Zhang, L. Ban, P. Chen, W. Du, X. Feng, B. F. Liu, *ACS Appl. Mater. Interfaces* **2017**, *9*, 27441; b) J. Wang, W. Li, Z. Lu, L. Zhang, Y. Hu, Q. Li, W. Du, X. Feng, H. Jia, B. F. Liu, *Nanoscale* **2017**, *9*, 15598.

[22] a) C. Jang, J. H. Lee, A. Sahu, G. Tae, *Nanoscale* **2015**, *7*, 18584; b) J. Qin, D. Chen, H. Hu, Q. Cui, M. Qiao, B. Chen, *Chem. Pharm. Bull.* **2007**, *55*, 1192.

[23] M. Delcea, N. Sternberg, A. M. Yashchenok, R. Georgieva, H. Bäumler, H. Möhwald, A. G. Skirtach, *ACS Nano* **2012**, *6*, 4169.

[24] a) J. P. Armstrong, M. N. Holme, M. M. Stevens, *ACS Nano* **2017**, *11*, 69; b) S. A. A. Kooijmans, L. A. L. Fliervoet, R. van der Meel, M. H. A. M. Fens, H. F. G. Heijnen, P. M. P. van Bergen en Henegouwen, P. Vader, R. M. Schiffelers, *J. Controlled Release* **2016**, *224*, 77.

[25] a) C. Alvarez-Lorenzo, L. Bromberg, A. Concheiro, *Photochem. Photobiol.* **2009**, *85*, 848; b) M. A. Azagarsamy, D. L. Alge, S. J. Radhakrishnan, M. W. Tibbitt, K. S. Anseth, *Biomacromolecules* **2012**, *13*, 2219; c) Y. Dai, H. Xiao, J. Liu, Q. Yuan, P. a. Ma, D. Yang, C. Li, Z. Cheng, Z. Hou, P. Yang, J. Lin, *J. Am. Chem. Soc.* **2013**, *135*, 18920; d) R. Huschka, A. Barhoumi, Q. Liu, J. A. Roth, L. Ji, N. J. Halas, *ACS Nano* **2012**, *6*, 7681; e) W. Li, X. Cai, C. Kim, G. Sun, Y. Zhang, R. Deng, M. Yang, J. Chen, S. Achilefu, L. V. Wang, Y. Xia, *Nanoscale* **2011**, *3*, 1724.

[26] T. Ta, T. M. Porter, *J. Controlled Release* **2013**, *169*, 112.

[27] a) X. H. Huang, I. H. El-Sayed, W. Qian, M. A. El-Sayed, *J. Am. Chem. Soc.* **2006**, *128*, 2115; b) Z. Li, H. Wang, Y. Chen, Y. Wang, H. Li, H. Han, T. Chen, Q. Jin, J. Ji, *Small* **2016**, *12*, 2731; c) C.-T. Lin, I. C. Lin, S.-Y. Sung, Y.-L. Su, Y.-F. Huang, C.-S. Chiang, S.-H. Hu, *Adv. Funct. Mater.* **2016**, *26*, 4169; d) Z.-Q. Zhang, S.-C. Song, *Biomaterials* **2016**, *106*, 13.

[28] X. Ma, J. Jia, R. Cao, X. Wang, H. Fei, *J. Am. Chem. Soc.* **2014**, *136*, 17734.

[29] a) R. M. Hoffman, *Breast Cancer Res.* **2013**, *15*, 310; b) A. Suetsugu, K. Honma, S. Saji, H. Moriwaki, T. Ochiya, R. M. Hoffman, *Adv. Drug Delivery Rev.* **2013**, *65*, 383.

[30] C. Murdoch, M. Muthana, S. B. Coffelt, C. E. Lewis, *Nat. Rev. Cancer* **2008**, *8*, 618.

[31] a) M. J. Haney, N. L. Klyachko, Y. Zhao, R. Gupta, E. G. Plotnikova, Z. He, T. Patel, A. Piroyan, M. Sokolsky, A. V. Kabanov, E. V. Batrakova, *J. Controlled Release* **2015**, *207*, 18; b) W. Zhang, Z.-L. Yu, H. Wu, J.-G. Ren, H.-F. Xia, G.-L. Sa, J.-Y. Zhu, D.-W. Pang, Y.-F. Zhao, G. Chen, *ACS Nano* **2017**, *11*, 277; c) S. C. Jang, O. Y. Kim, C. M. Yoon, D. S. Choi, T. Y. Roh, J. Park, J. Nilsson, J. Lotvall, Y. K. Kim, Y. S. Gho, *ACS Nano* **2013**, *7*, 7698.

[32] E. Jin, B. Zhang, X. Sun, Z. Zhou, X. Ma, Q. Sun, J. Tang, Y. Shen, E. Van Kirk, W. J. Murdoch, M. Radosz, *J. Am. Chem. Soc.* **2013**, *135*, 933.

[33] N. Lozano, W. T. Al-Jamal, A. Taruttis, N. Beziere, N. C. Burton, J. Van den Bossche, M. Mazza, E. Herzog, V. Ntziachristos, K. Kostarelos, *J. Am. Chem. Soc.* **2012**, *134*, 13256.

[34] P. Li, M. Kaslan, S. H. Lee, J. Yao, Z. Gao, *Theranostics* **2017**, *7*, 789.